JACS
JOURNAL OF THE AMERICAN CHEMICAL SOCIETY

Article

pubs.acs.org/JACS

Carbon Nanotubes as Electrically Active Nanoreactors for Multi-Step Inorganic Synthesis: Sequential Transformations of Molecules to Nanoclusters and Nanoclusters to Nanoribbons

Akos Botos,[†] Johannes Biskupek,[‡] Thomas W. Chamberlain,[†,§] Graham A. Rance,[†] Craig T. Stoppiello,[†] Jeremy Sloan,[∥] Zheng Liu,[⊥,#] Kazutomo Suenaga,[⊥] Ute Kaiser,[‡] and Andrei N. Khlobystov*[,†]

[†]School of Chemistry, University of Nottingham, University Park, Nottingham NG7 2RD, United Kingdom

[‡]Central Facility of Electron Microscopy, Electron Microscopy Group of Materials Science, Albert-Einstein-Allee 11, D-89081 Ulm, Germany

[§]Institute of Process Research Development, School of Chemistry, University of Leeds, Leeds LS2 9JT, United Kingdom

[∥]Warwick Centre for Analytical Science, Department of Physics, University of Warwick, Coventry CV4 7AL, United Kingdom

[⊥]Nanomaterials Research Institute, National Institute of Advanced Industrial Science and Technology (AIST), Tsukuba 305-8565, Japan

[#]Inorganic Functional Materials Research Institute National, Institute of Advanced Industrial Science and Technology (AIST), Nagoya 463-8560, Japan

Supporting Information

ABSTRACT: In organic synthesis, the composition and structure of products are predetermined by the reaction conditions; however, the synthesis of well-defined inorganic nanostructures often presents a significant challenge yielding nonstoichiometric or polymorphic products. In this study, confinement in the nanoscale cavities of single-walled carbon nanotubes (SWNTs) provides a new approach for multistep inorganic synthesis where sequential chemical transformations take place within the same nanotube. In the first step, SWNTs donate electrons to reactant iodine molecules (I_2), transforming them to iodide anions (I^-). These then react with metal hexacarbonyls ($M(CO)_6$, M = Mo or W) in the next step, yielding anionic nanoclusters $[M_6I_{14}]^{2-}$, the size and composition of which are strictly dictated by the nanotube cavity, as demonstrated by aberration-corrected high resolution transmission electron microscopy, scanning transmission electron microscopy, and energy dispersive X-ray spectroscopy. Atoms in the nanoclusters $[M_6I_{14}]^{2-}$ are arranged in a perfect octahedral geometry and can engage in further chemical reactions within the nanotube, either reacting with each other leading to a new polymeric phase of molybdenum iodide $[Mo_6I_{12}]_n$ or with hydrogen sulfide gas giving rise to nanoribbons of molybdenum/tungsten disulfide $[MS_2]_n$ in the third step of the synthesis. Electron microscopy measurements demonstrate that the products of the multistep inorganic transformations are precisely controlled by the SWNT nanoreactor with complementary Raman spectroscopy revealing the remarkable property of SWNTs to act as a reservoir of electrons during the chemical transformation. The electron transfer from the host nanotube to the reacting guest molecules is essential for stabilizing the anionic metal iodide nanoclusters and for their further transformation to metal disulfide nanoribbons synthesized in the nanotubes in high yield.

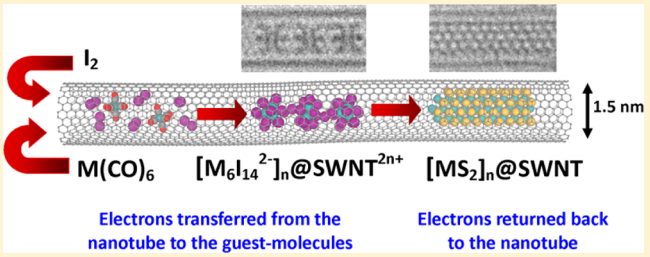

INTRODUCTION

Single-walled carbon nanotubes (SWNTs) are among the most effective and universal containers for molecules. Provided that the internal diameter of the host nanotube is wider than the critical diameter of the guest molecule, the insertion of molecules into SWNT is spontaneous and, in some cases such as fullerenes and their derivatives, irreversible due to the ubiquitous van der Waals forces dominating the host−guest interactions between the nanotube and molecules.[1] Fullerenes[2,3] or organic molecules[4−10] encapsulated in SWNT can then be triggered to react inside the nanotube to form unusual oligomers and polymers,[11−13] graphene nanoribbons,[14−16] nanotubes,[8,17] or extraordinary molecular nanodiamonds.[9] These examples clearly demonstrate the use of SWNT as nanoscale chemical reactors, where the structure of the macromolecular product can be precisely controlled by spatial confinement of the reactions in the nanotube channel.

In contrast to organic molecules, the controlled chemical transformations of inorganic compounds in SWNT are significantly less explored. The challenges of inorganic synthesis in nanotubes are exemplified by metal hexacarbonyl complexes

Received: April 8, 2016
Published: June 3, 2016

DOI: 10.1021/jacs.6b03633
J. Am. Chem. Soc. 2016, 138, 8175−8183

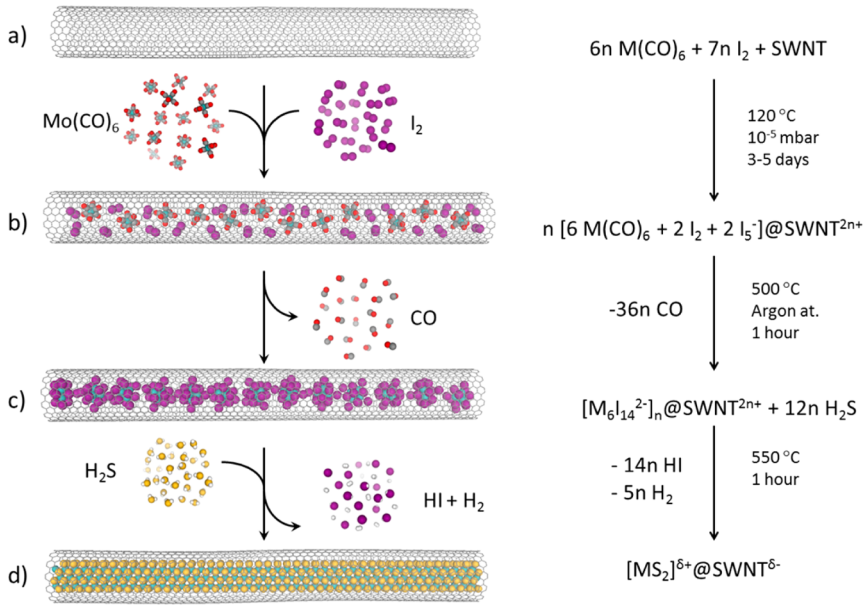

Figure 1. Multistep inorganic synthesis performed in carbon nanotubes: (a) the encapsulation and (b) conversion of the metal carbonyl and iodine molecules into (c) metal iodide nanoclusters $[M_6I_{14}]^{2-}$, where M = Mo or W, followed by (d) the reaction of the nanoclusters with H_2S yielding metal sulfide nanoribbons $[MS_2]_n$, where M = Mo or W (for WS_2 $\delta < 1$ and for MoS_2 $\delta = 0$).

$M(CO)_6$ (where M is a transition metal)—these geometrically ideal guest molecules for nanotubes with diameters between 1.3 and 1.5 nm readily convert at elevated temperatures into metallic nanoclusters consisting of 30—60 metal atoms inside SWNT, possessing a clean surface and unprecedented stability for such tiny sizes, interacting strongly with the nanotube interior,[18−20] and showing promise for applications in catalysis.[21] Unfortunately, metallic bonding lacks directionality and is highly labile compared to covalent bonding, generally resulting in a nonuniform distribution of sizes and variations in the shapes of the metal clusters synthesized in SWNT,[18] which is in stark contrast to the well-defined products synthesized from organic molecules in SWNT. At this tiny scale (nm or subnm cluster diameters), any structural inhomogeneity in the sample inevitably leads to nonuniform physicochemical properties because even the smallest changes in the size and shape of the clusters will have drastic effects on their properties.[22] As a consequence, a complete understanding of the mechanisms of the nanocluster—nanotube interactions is significantly hindered,[19,20] and thus any development of the practical applications of metal nanoclusters in nanotubes, such as in catalysis or electronic devices, is severely compromised by the lack of a well-defined structural interface between the host nanotube and guest molecules.

Although SWNTs are already used as very effective nanoreactors for organic reactions where the chemo-, regio-, or enantioselectivity can be tuned as a result of confinement in carbon nanotubes,[23−25] inorganic synthesis in carbon nanotubes yielding materials with well-defined elemental composition, stoichiometry, and structure still remains a significant challenge[26] with all currently known inorganic reactions in SWNT producing either polymeric ionic crystals of $[M_xA_y]_n$ type, where M is a cation and A is an anion, of varied lengths and widths (determined primarily by the dimensions of the nanotube), or discrete clusters with poorly defined size and shape, similar to those of transition metals mentioned above. In this study, we perform the first multistep inorganic synthesis inside carbon nanotubes. We demonstrate that the products are synthesized with atomically precise stoichiometry in the SWNT cavity and discover the unexpected ability of the nanotube to act as an electrically active host structure during the synthesis—a new feature of SWNTs in the context of nanoreactors—which appears to be essential for the stabilization of the ionic products of the reaction.

To explore the potential for the assembly of inorganic nanoclusters with well-defined structure and composition, we introduced an additional element, iodine, into SWNT with the encapsulated metal carbonyl complex $M(CO)_6$ (M = W or Mo; Figure 1b). Being significantly more directional than metal—metal bonding, the metal—halogen bonds are expected to direct the atoms into well-structured nanoclusters with a more strictly defined shape, size, and atomic structure than in the case of metallic clusters. In contrast to $M(CO)_6$ that interacts with SWNT by van der Waals forces with little or no contribution of electron transfer, the electron-accepting halogen I_2 is known to withdraw a substantial amount of electronic density from the nanotube,[27,28] thus causing a significant blue-shift of the G-mode in the Raman spectra of SWNT cofilled with $M(CO)_6$ and I_2 in our experiments (Figures 2m and 3j). As a result, some I_2 guest molecules convert to polyiodide chains of the I_n^- within SWNT that contribute new low-frequency Raman bands (Figures 2l and 3k) in the range between 100 and 110 cm^{-1}, which is consistent with the previous observations for polyiodides in SWNT.[27,28] Therefore, SWNT cofilled with $M(CO)_6$ and I_2 can be described more accurately as $m\cdot[M(CO)_6 + I_n^-]@SWNT^{m+}$, so that the host nanotube serves not only as a container for the molecules but also as a donor of electrons. The coconfinement of hexacarbonyl complexes with metal atoms in the oxidation state of zero and polyiodide within same narrow channel of SWNT creates an ideal starting point for an inorganic chemical reaction between the metal and halogen. Indeed, a small temperature increase triggers a drastic chemical transformation in $m\cdot[M(CO)_6 + I_n^-]@SWNT^{m+}$ (Figure 1b,c) as indicated by clear changes in the Raman spectra, where the bands associated with polyiodide are replaced by a new set of bands at lower

DOI: 10.1021/jacs.6b03633
J. Am. Chem. Soc. 2016, 138, 8175−8183

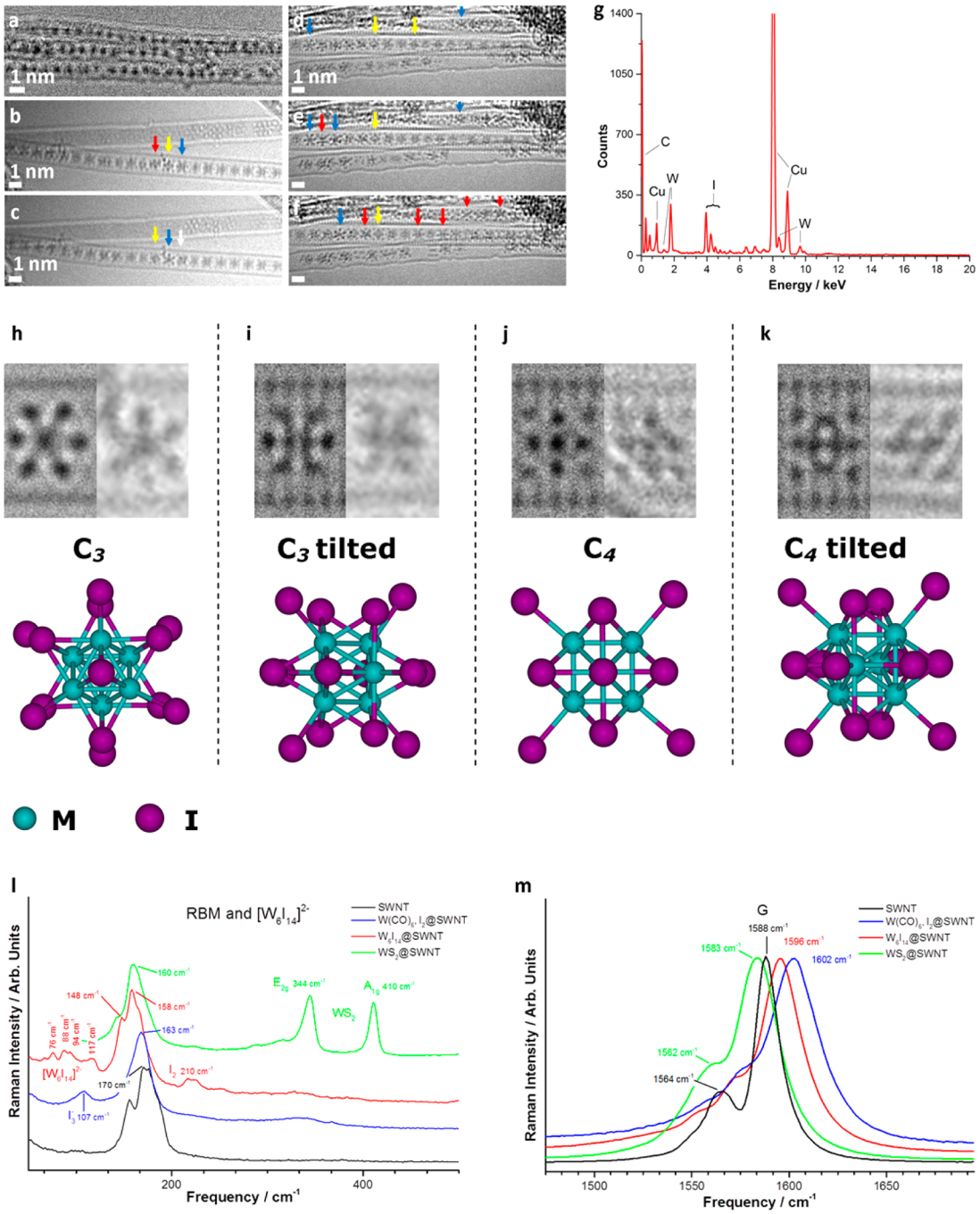

Figure 2. (a) HRTEM at 100 kV and (b–f) AC-HRTEM at 80 kV images of $n{\cdot}[W_6I_{14}]^{2-}$@SWNT^{2n+} demonstrating the tumbling motion of metal clusters over time (marked by arrows). (g) The EDX spectrum confirms the elemental composition of the clusters. Please note that the Cu peaks are due to the TEM specimen grid. (h–k) High magnification images of the four principal projections of octahedral $[W_6I_{14}]^{2-}$ and their corresponding atomic models. (l) Raman spectra in the low-frequency region showing the bands of the products formed inside the nanotubes at each stage of the multistep synthesis (polyiodide chains, blue; $[W_6I_{14}]^{2-}$ nanoclusters, red; $[WS_2]_n$ nanoribbons, green) and (m) a strong blue shift of the Raman G-band of SWNT indicative of the positive charge on SWNT due to the electron transfer to the guest species polyidide chains (blue) or metal iodide nanoclusters (red). A small red shift of the G band in the case of $[WS_2]_n$@SWNT (green) indicates the further transfer of electrons from the $[WS_2]_n$ nanoribbon to the SWNT, i.e., the formation of $[WS_2]_n^{\delta+}$@SWNT$^{\delta-}$, consistent with the known electron donor properties of WS_2.

frequencies, indicating the formation of new inorganic species in SWNT nanoreactors (Figures 2l and 3k). High-resolution transmission electron microscopy (HRTEM) imaging of nanotubes after the heat treatment reveals chains of discrete 1 nm clusters uniformly distributed along the nanotube channel (Figure 2a and 3a), which are in stark contrast to the irregular metallic clusters randomly positioned in SWNT that form from $M(CO)_6$ under similar conditions.[18] Aberration-corrected (AC) HRTEM imaging demonstrates a surprisingly well-defined atomic structure of the nanoclusters with a polyhedral geometry, which appears to be virtually the same for Mo- and W-containing species (Figures 2h–k and 3c–g). Energy dispersive X-ray (EDX) spectra recorded for small bundles (3–5 nanotubes) filled with the nanoclusters indicates the atomic ratio of M:I to be approximately 3:7 (Figures 2g and 3i), and time-series imaging shows that the metal iodide nano-

DOI: 10.1021/jacs.6b03633
J. Am. Chem. Soc. 2016, 138, 8175–8183

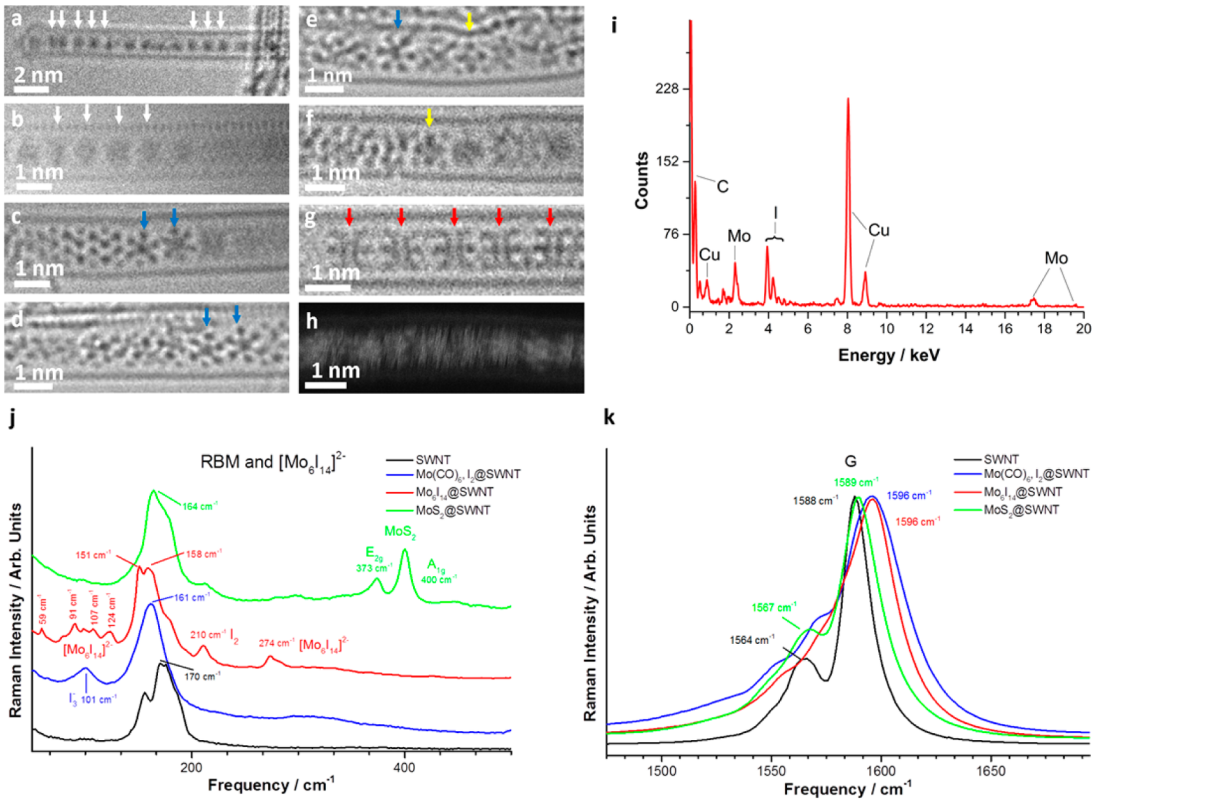

Figure 3. (a) HRTEM at 100 kV and (b–g) AC-HRTEM at 80 kV images of $n\cdot[Mo_6I_{14}]^{2-}$@SWNT^{2n+} demonstrating the tumbling motion of metal clusters over time (marked by arrows) and (h) a scanning transmission electron microscopy (STEM) annular dark field (ADF) image taken at 60 kV illustrating the presence of heavy elements inside the nanotube. Please note that the fast motion of the nanoclusters during the slow STEM acquisition leads to unavoidable smearing and blurring of the contrast. (i) The EDX spectrum confirms the elemental composition of the clusters. Please note that the Cu peaks are due to the TEM specimen grid. (j) Raman spectra in the low-frequency region show bands of the products formed inside the nanotube at each stage of the multistep synthesis (polyiodide chains, blue; $\cdot[Mo_6I_{14}]^{2-}$ nanoclusters, red; $[MoS_2]_n$ nanoribbons, green) and (k) the blue shift of the Raman G-band of the nanotube indicating the positive charge on the SWNT due to the electron transfer to the polyiodide and nanocluster guest species. No electron transfer is observed for $[MoS_2]_n$@SWNT relative to that for SWNT.

clusters freely translate and rotate within the nanotube, behaving as discrete species and not bonded to each other. Such behavior is surprising because metal iodides typically form polymeric structures due to the tendency of iodide anions to bridge between metal atoms within the crystal, including metal iodide crystals inside nanotubes.[29,30] The apparent unrestricted tumbling of the metal iodide nanoclusters in SWNT is different to the dynamics of metallic clusters under the same conditions that usually exhibit a slower motion,[18,19] thus making imaging of the atomic structures of metal iodides challenging, particularly in the case of Mo (Figure 3b). However, the tumbling motion of the nanoclusters can be beneficial for understanding their 3D structures in HRTEM analysis, as a rotating nanocluster allows direct visualization of all of its principal projections by time-series imaging of the same cluster within the nanotube (Figure 2b–f) without any need to tilt the specimen. Extensive AC-HRTEM image acquisition combined with structural modeling and HRTEM image simulations (Supporting Information) strongly indicate a highly symmetrical octahedral arrangement of the metal atoms with eight μ^3-I bridging I atoms capping each face of the octahedron, and a further six μ^1-I atoms coordinated to each metal (Figure 2h–k), yielding a shape topologically similar to polyoxometalate (POM) clusters[31,32] and an overall stoichiometry M_6I_{14} agreeing well with the EDX elemental analysis. The new set of low-frequency Raman bands in the 50–130 cm^{-1} range emerging as a result of polyiodide and metal complex reaction in SWNT is consistent with the anionic form of the clusters $[W_6I_{14}]^{2-}$ (Figure 2l) and $[Mo_6I_{14}]^{2-}$ (Figure 3k), whereas the G-band is significantly blue-shifted for both clusters with respect to the empty nanotubes (Figures 2m and 3k), suggesting that the electrons abstracted from SWNT by iodine in the first step of the inorganic synthesis have been passed onto the metal iodide nanocluster such that the host nanotube remains positively charged, and the overall structure is described as $n\cdot[M_6I_{14}]^{2-}$@SWNT^{2n+} (Figure 1c). A typical nanotube with an average diameter of 1.4 nm utilized in these experiments provides a near ideal fit for anionic $[M_6I_{14}]^{2-}$ clusters and simultaneously acts as a counterion balancing the charge with the terminal μ^1-I atoms engaged in direct contact with the inner SWNT sidewall (Figure 1). Because the μ^1-I atoms are not expected to form any directional interactions with the sp^2-carbon atoms of the SWNT, the energy difference between dissimilar orientations of $[M_6I_{14}]^{2-}$ is not expected to be sufficiently high to hinder the tumbling motion of the nanoclusters observed in time-series HRTEM imaging (Supporting Videos 1 and 2).

The EDX spectra of the metal iodide nanoclusters in nanotubes clearly distinguish W and Mo in $n\cdot[W_6I_{14}]^{2-}$@SWNT^{2n+} (Figure 2g) and $n\cdot[Mo_6I_{14}]^{2-}$@SWNT^{2n+} (Figure 3i), respectively, but the two types of clusters are structurally indistinguishable in HRTEM images due to the very similar ionic diameters of Mo and W, leading to near identical lengths of W–I and Mo–I bonds and thus the

DOI: 10.1021/jacs.6b03633
J. Am. Chem. Soc. 2016, 138, 8175–8183

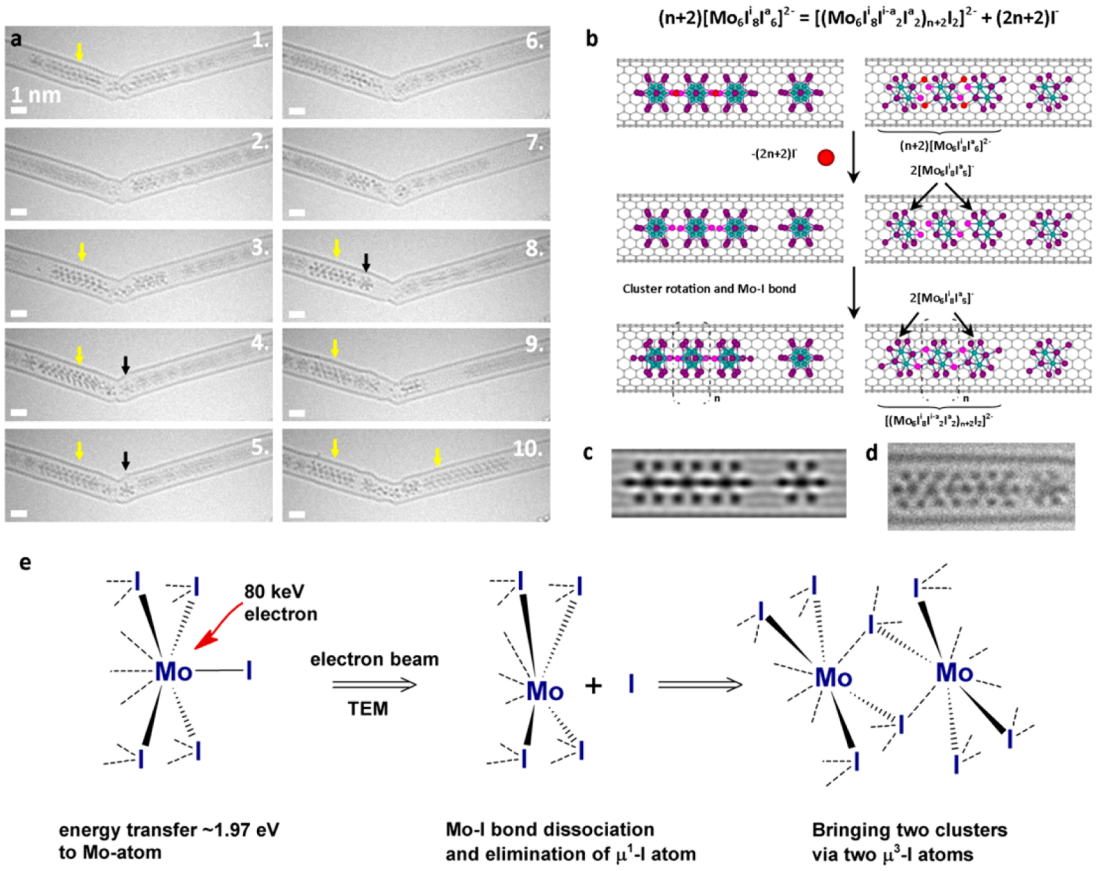

Figure 4. (a) AC-HRTEM at 80 kV time series images showing the transformation of $n{\cdot}[Mo_6I_{14}]^{2-}$@SWNT^{2n+} to $[Mo_6I_{12}]_n$@SWNT (yellow arrows) under 80 keV e-beam. (b) Structural diagram of a reaction of iodide elimination and formation of the polymeric form of molybdenum iodide $[Mo_6I_{12}]_n$. (d) High magnified 80 kV AC-HRTEM images of $[Mo_6I_{12}]_n$@SWNT and (c) corresponding image simulation. (e) Schematic diagram illustrates the kinetic energy transfer from the incident 80 keV electron to the Mo atom (up to 1.97 eV according to eq 1), which can trigger the dissociation of the Mo−I bond with μ^1-I followed by μ^3-I linking of the neighboring clusters and thus leading to the polymeric molybdenum iodide structure $[Mo_6I_{12}]_n$ observed in AC-HRTEM.

same sizes and shapes of the $[W_6I_{14}]^{2-}$ and $[Mo_6I_{14}]^{2-}$ clusters. Interestingly, detailed comparison of the motion of the nanoclusters highlights significant differences in their dynamic behaviors under the 80 keV electron beam: after extensive irradiation, $[Mo_6I_{14}]^{2-}$ appears to transform from discrete, highly mobile clusters into a static polymeric structure (Figure 4a and Supporting Video 2), whereas $[W_6I_{14}]^{2-}$ remains largely unchanged under similar conditions (Supporting Video 1). Recently, we have demonstrated that the electron beam of the TEM can play the role of an effective stimulus of chemical transformations, primarily due to the transfer of kinetic energy from the fast electrons of the e-beam to the atoms of the molecule.[19,20,33] Generally, if the amount of transferred energy from the e-beam to an atom exceeds the threshold of displacement of the atom and dissociation of the chemical bonds, the atom is knocked out of the molecule[34] and a chain of chemical transformations is triggered by the e-beam.

$$T = \frac{2{\cdot}M{\cdot}E(E + 2m_e{\cdot}c^2)}{(M + m_e)^2{\cdot}c^2 + 2M{\cdot}E} \quad (1)$$

The maximum amount of energy transferred from the e-beam to the atom (T) depends on the energy of incident electrons (E), which is controlled by the accelerating voltage of the TEM (80 kV in our case). Most importantly, T is inversely proportional to the atomic weight of the element (M), so that under typical TEM imaging conditions, lighter elements within the molecule are significantly more susceptible to the knock-on effect, as demonstrated for example for the protium and deuterium isotopes of hydrogen in organic molecules[31] (other parameters in eq 1 are mass of electron (m_e) and speed of light (c)).

Specifically, because Mo is a significantly lighter atom than W or I, it receives the highest amount of kinetic energy of 1.97 eV from the e-beam as compared to only 1.03 eV for W or 1.00 eV for I. The main outcome of the fact that twice as much energy is transferred from the e-beam to Mo as compared to that to W is a significantly increased likelihood for Mo to be displaced by the 80 keV e-beam from its equilibrium position in the metal iodide nanocluster (Figure 4e) and, thus, a potential rupture of Mo−I bonds, the weakest of which is the single bond with the terminal μ_1-I atom (Figure 4b). A coordinatively unsaturated Mo cation formed in this process requires completion of its coordination environment, which can be achieved by sharing a μ^3-I atom of a neighboring cluster (Figure 4e), which in effect leads to the polymerization of discrete $[Mo_6I_{14}]^{2-}$ clusters into a continuous crystal with a repeating unit $[Mo_6I_{12}]_n$ (Figure 4c,d). Such a structure is not known for any form of molybdenum iodide in the bulk form, and topologically, $[Mo_6I_{12}]_n$ is much closer to the polymeric mixed molybdenum iodides/sulfides $Mo_6S_xI_y$, where S atoms substitute some of the I atoms in the coordination sphere of Mo.[35−37] Therefore, the formation of $[Mo_6I_{12}]_n$@SWNT observed in AC-HRTEM is a

DOI: 10.1021/jacs.6b03633
J. Am. Chem. Soc. 2016, 138, 8175−8183

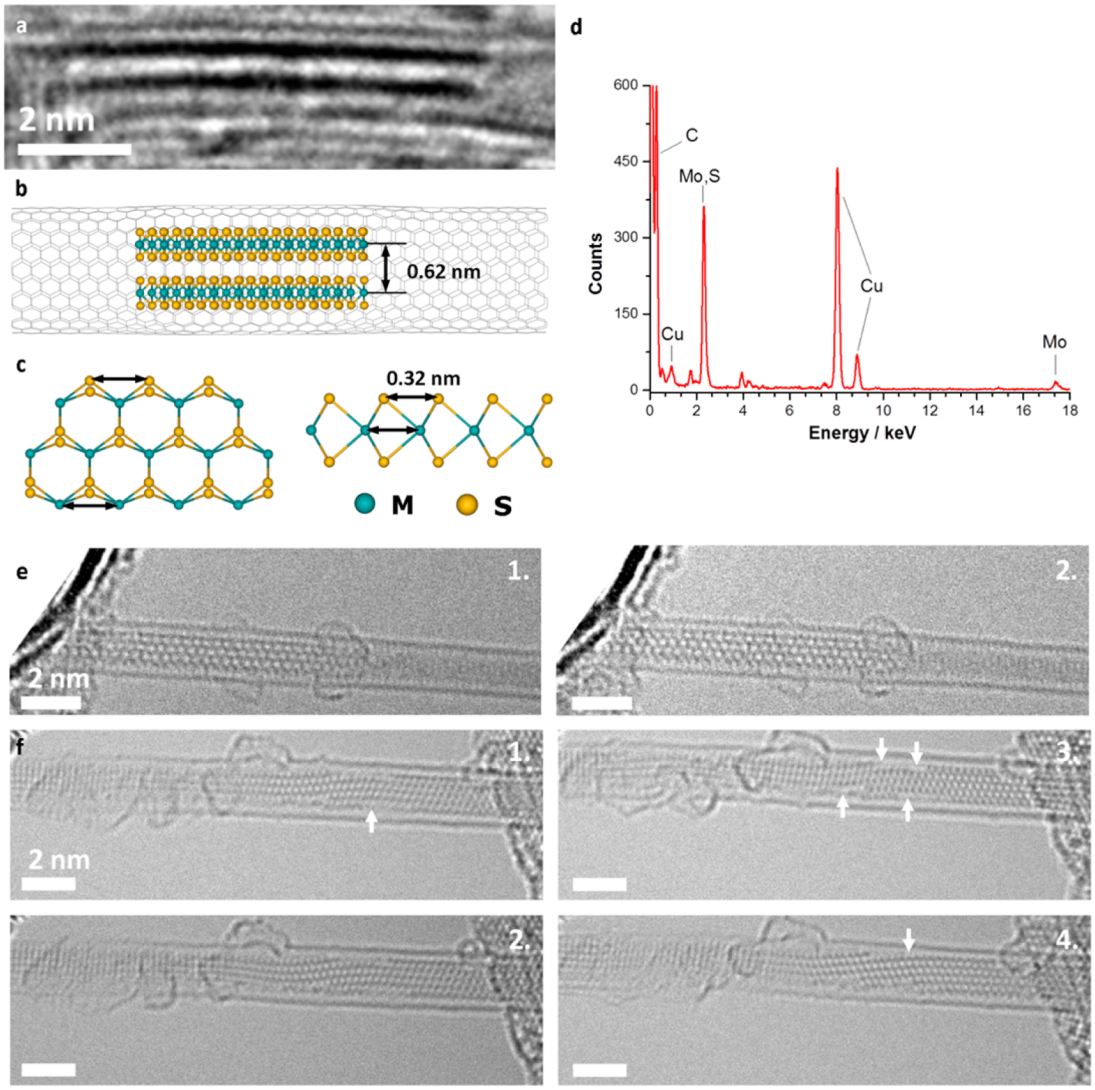

Figure 5. (a) HRTEM at 100 kV image of $[MoS_2]_n$@SWNT with the nanoribbon in edge-on orientation. Structural diagrams of $[MoS_2]_n$ in (b) edge-on and (c) face-on orientations. (d) The EDX spectrum confirms the composition of the nanoribbon in the nanotube as MoS_2. Please note that the Cu peaks are due to the TEM specimen grid. High magnification 80 kV AC-HRTEM micrographs illustrating a nanoribbon with (e) a perfect zigzag edge and (f) a defective zigzag edge undergoing structural transformations under the e-beam. The white arrows indicate positions of structural defects in the nanoribbon.

combined result of the knock-on effect of the e-beam and the confinement effect of the nanotube directing the growth of this unusual structure.

The highly dynamic behavior of the metal iodide nanoclusters and the structural transformation of $[Mo_6I_{14}]^{2-}$ under the e-beam clearly indicates that these guest species can be activated for further chemical transformations inside the nanotubes. Spatial restriction of the internal cavity of SWNT has previously been employed as a powerful template to direct chemical reactions along a specific pathway,[5−17] but with the size of the metal iodide nanocluster effectively filling the entire cross-section (Figures 2 and 3), there is a risk of blocking the SWNT channel, which would severely hinder the diffusion of any other reactant into the nanotube and thus potentially prohibit any further chemical transformations within the SWNT. For the potential for multistep chemical reactions within the SWNT nanoreactor to be assessed, H_2S gas has been introduced into $n\cdot[M_6I_{14}]^{2-}$@$SWNT^{2n+}$ (Figure 1c,d). Despite the fact that the nanotubes are densely filled with metal iodide clusters with no physical space available for H_2S to enter and pass between the nanoclusters, the clusters transform into continuous nanoribbon-shaped sulfides $[MoS_2]_n$ (Figure 5a,e,f) and $[WS_2]_n$ (Figure 6a−c) with remarkable efficiency, where virtually all of the metal iodide nanoclusters are converted into the metal sulfide nanoribbons according to EDX and HRTEM (Figure 6) even after 1 h of exposure to H_2S. Molybdenum and tungsten sulfide nanoribbons have recently attracted significant attention due to a range of functional electronic properties. In our experiments, the transformation of $n\cdot[M_6I_{14}]^{2-}$@$SWNT^{2n+}$ to $[MS_2]_n$@SWNT proceeds smoothly and efficiently with no loss of material from SWNT and with most of the nanotubes filled with well-ordered crystalline structures of hexagonal MoS_2 and WS_2 (Figures 5 and 6, Supporting Video 3) similar to those reported in the literature.[38,39] The width of the nanoribbon is strictly controlled by the nanotube diameter with their edges adopting a perfect zigzag conformation in most cases (Figures 5e and 6a), but occasional edge defects were found in some nanoribbons (Figure 5f). It is logical to suggest that the H_2S gas

DOI: 10.1021/jacs.6b03633
J. Am. Chem. Soc. 2016, 138, 8175−8183

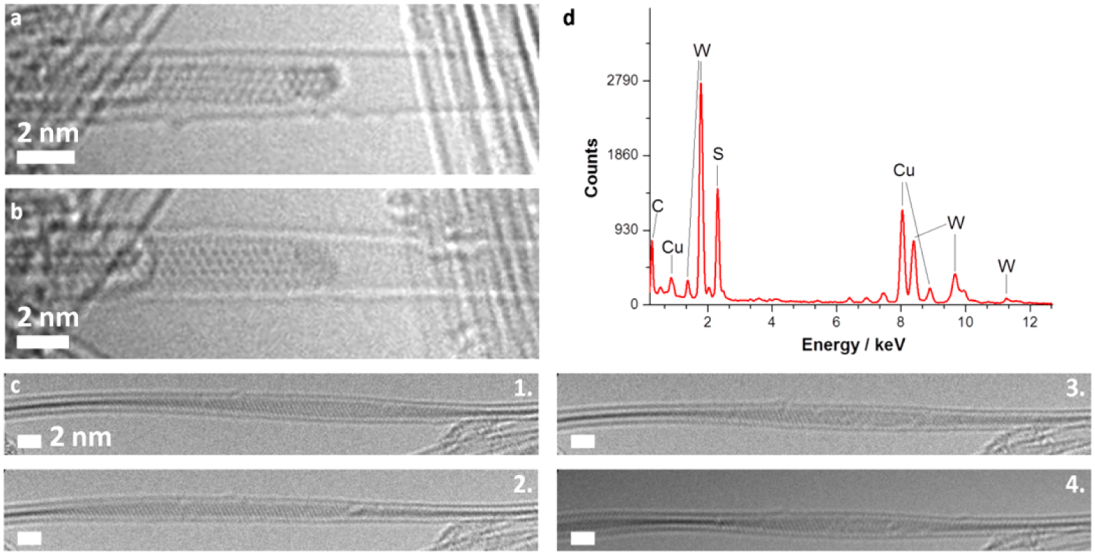

Figure 6. (a,b) AC-HRTEM images showing $[WS_2]_n$@SWNT and (c) a time series of images illustrating the rotation of the nanoribbon inside the nanotube. (d) EDX spectrum confirming the elemental composition of the nanoribbon.

starts reacting with $[M_6I_{14}]^{2-}$ nanoclusters positioned at the termini of SWNT, so that two $[MS_2]_n$ nanoribbons grow from the termini of SWNT toward the nanotube center. Naturally, any discrepancies in the initial growth conditions of the two nanoribbons propagating toward each other would lead to an incommensurate structure at the point they merge, resulting in a twisted defect, such as that observed in Figure 5f. The edge defect is caused by a mismatch of the nanoribbon structures on the left and on the right (Figure 5f), and appears to be unable to anneal due to the space limitation imposed by the host nanotube remaining highly dynamic with the nanoribbon atoms continually changing between the structure of $[MS_2]_n$ with rows of hexagons parallel to the SWNT axis (frame 3, Figure 5f) and $[MS_2]_n$ with twisted rows of hexagons (frame 4, Figure 5f) due to the presence of under-coordinate labile metal atoms (Supporting Video 3). In contrast, the defect-free zigzag edges remain almost completely static under similar conditions.

EDX spectroscopy confirms almost complete removal of the iodine atoms from the nanotubes in the final step of the synthesis and shows the atomic ratio of metal to sulfur as 1:2, supporting the formation of stoichiometric metal sulfides within SWNT. The negatively charged metal iodide nanoclusters formed in the second step of the synthesis require the host nanotube to donate electrons and to become positively charged to balance the negative charges of the guest species, which leads to the significant blue shift of the SWNT G-band observed by Raman spectroscopy (Figures 2m and 3k). However, unlike $[M_6I_{14}]^{2-}$ nanoclusters, $[MS_2]_n$ nanoribbons are essentially charge-neutral, such that no electronic contribution of SWNT is required to balance the charge of the guest species (Figure 1d). Indeed, upon formation of $[MoS_2]_n$@SWNT, the G-band of the nanotubes is shifted back to its original position as it was in empty SWNT, which indicates no electron transfer from SWNT to $[MoS_2]_n$ or vice versa. Interestingly, in the case of tungsten disulfide, we observe a small red shift of the G-band of the nanotubes subsequent to the formation of $[WS_2]_n$@SWNT relative to the empty nanotube, indicating a small but measurable partial transfer of electrons from the electron donor guest-$[WS_2]_n$ nanoribbon to the now electron-acceptor SWNT. This indicates that, unlike MoS_2, WS_2 acts as a weak electron donor to the nanotube consistent with the reported differences in the valence band maximum levels and thus propensity of the metal sulfide to donate electrons to the nanotube, where WS_2 has been calculated to be 0.39 eV higher than MoS_2.[40] In either case, the electrons "borrowed" from the host nanotube by polyiodide chains in the first step (Figure 1a,b) appear to be critically important for the stabilization of anionic $[M_6I_{14}]^{2-}$ nanoclusters in the second step (Figure 1c) but are effectively returned back to the host nanotube in the third step of the reaction where $[M_6I_{14}]^{2-}$ convert to effectively charge-neutral $[MS_2]_n$ (or slightly positively charged in the case of $[WS_2]_n^{\delta+}$) (Figure 1d). This demonstrates a remarkable property of carbon nanotubes to act not only as nanoreactors constraining the space around the chemical reaction and templating the formation of nanoclusters or the growth of nanoribbons but also as electrically active host structures, lending their electrons when they are required for a chemical reaction to occur inside SWNT and retrieving electrons back when they are no longer required by the guest species.

In summary, carbon nanotubes are becoming an increasingly important class of nanoscale containers and reactors, where the pathways of chemical reactions can change significantly as a result of the restricted space of the reaction[5−17] or due to the interactions between the reactant molecules or catalyst particles with the host nanotube.[23,24] Being highly conducting and having a symmetric distribution of filled and empty electronic states, SWNTs possess remarkable electric properties and a unique ability to donate or accept electrons, which make nanotubes distinct among other nanocontainers and nanoreactors. Even subtle electron transfer between a catalyst and carbon nanotube, for example, has the potential to change the rates or selectivities of single-step chemical reactions.[41] In this study, we carried out the first multistep synthesis within a carbon nanotube by transforming molecules ($M(CO)_6$ and I_2) to nanoclusters ($[M_6I_{14}]^{2-}$) and subsequently nanoclusters to nanoribbons ($[MS_2]_n$) within the cavity of the same nanotube. A combination of HRTEM imaging, EDX, and Raman spectroscopy was employed to follow the multistep synthesis inside the nanotube to reveal that the SWNT is engaged in significant electron transfer with the guest species at different

DOI: 10.1021/jacs.6b03633
J. Am. Chem. Soc. 2016, 138, 8175−8183

stages of the synthesis, which is necessary to promote the reactions. SWNTs serve as reservoirs of electrons that can be donated to the products of the reactions (e.g., nanoclusters), stabilizing them within the SWNT cavity and thus improving the efficiency of their formation and subsequent conversion to MS_2 nanoribbons in the final stage of the multistep synthesis. We have found the direct synthesis of $[MS_2]_n$@SWNT from $M(CO)_6$@SWNT to be significantly less efficient, leading to only a small number of nanotubes (~5%) with $[MS_2]_n$ nanoribbons, as at elevated temperatures metal carbonyl molecules interacting with the SWNT by weak van der Waals forces are significantly more likely to exit from the SWNT channel than the $[M_6I_{14}]^{2-}$ nanoclusters held within the nanoreactors by strong Coulombic forces. The demonstration of active electric participation of the host nanotube in the chemical reactions of the guest species can be harnessed to direct the synthesis of desired products and in the future can be employed to design and fabricate new types of inorganic materials with precisely controlled structure and properties. The development of new methodologies for the efficient removal of inorganic products from the host nanotubes, for example, based on the extraction of the products or the selective oxidation of SWNT, may be seen as the next important challenge in this field of research. However, electronically, optically, and magnetically active inorganic nanostructures fabricated within the nanoscale containers, such as SWNT in our study, are already "prepackaged" for a wealth of new practical applications, for example, in catalysis and electrocatalysis, field-effect transistors, sensors, and spintronic devices, where the host nanotube connects the inorganic guest nanostructures with the macroworld and thus enables efficient harnessing of their functional properties.

EXPERIMENTAL SECTION

Materials. Arc-discharge SWNTs (average d_{NT} = 1.4 nm, purity 90%) were purchased from Helix Material Solutions. Mo and W hexacarbonyls (purity ≥98 and 99%, respectively) were purchased from Acros Organics. I_2 (purity ≥99.8%) and H_2S gas (purity ≥99.5%) were purchased from Fischer Scientific and Sigma-Aldrich, respectively, and all reagents were used without further purification.

Encapsulation of $M(CO)_6$ or $M(CO)_6$ and I_2 Together into CNTs. SWNTs were heated in air at 380 °C for 20 min to open their closed ends and remove any adsorbed water. Freshly opened SWNTs (5 mg) were mixed with a large excess of precursor molecules, i.e., $M(CO)_6$ or $M(CO)_6$ and I_2 (M = Mo, W), and the resultant mixture was sealed in a Pyrex glass vessel (d = 10 mm, l = 10 cm) under high vacuum (10^{-6} mbar). The sealed vessel was placed into a preheated box furnace (120 °C) for several days depending on the experiment. Prior to opening, the Pyrex glass vessel was taken out from the furnace and cooled by immersing it in an ice-water bath for 5 min.

Chemical Transformation of $M(CO)_6$ and I_2 Precursor Molecules into $[M_6I_{14}]^{2-}$ in CNTs. The SWNTs containing $M(CO)_6$ and I_2 precursor molecules were sealed in a Pyrex glass vessel, which was first evacuated (10^{-6} mbar) and then filled with Ar gas (0.7 bar). The sealed Pyrex glass tube was then transferred into a preheated furnace (500 °C). After an hour, the sample was taken out from the furnace and left on an asbestos tile to cool to room temperature.

Formation of $[MS_2]_n$ Nanoribbons in SWNTs with H_2S Gas. The SWNTs containing $M(CO)_6$ or $M(CO)_6$ and I_2 precursor molecules were transferred into a quartz boat and placed into a closed ceramic working tube (d = 25 mm, l = 60 cm) located within a tube furnace. In a typical experiment, the system was purged at room temperature with Ar and then H_2S for 1 h each at ~15 mL/min. The furnace was heated to the desired reaction temperature, typically 550 °C (25 °C/min), which was maintained along with a moderate (~15 mL/min) H_2S gas flow for 2 h. Then, the furnace was cooled (25 °C/min) to room temperature under Ar gas flow. The exhaust of the system was released into the fume hood through a bleach bath to neutralize any excess H_2S.

Transmission Electron Microscopy and Energy-Dispersive X-ray Spectroscopy. Prior to investigation, the carbon nanotube samples (~0.5 mg) were dispersed in isopropyl alcohol (2 mL) using an ultrasonic bath (~15 min). Subsequently, a few drops were dropcast onto a copper TEM grid coated with lacy carbon film (Agar Scientific) to support the carbon nanotubes.

Conventional TEM images and EDX spectra were acquired with a JEOL 2100F microscope with a Schottky electron gun operated at 100 kV accelerating voltage at the Nottingham Nanotechnology and Nanoscience Centre, University of Nottingham, UK.

Aberration-corrected high-resolution TEM analysis was carried out on an imaging-side aberration-corrected (CEOS-type hexapole corrector) FEI Titan 80-300 transmission electron microscope operated at 80 kV at the Central Facility of Electron Microscopy, Ulm University, Germany, and scanning transmission electron microscopy (STEM) imaging was performed on a JEOL 2100F with a cold field-emission gun and an aberration DELTA-corrector for the illumination system operated at 60 kV at the National Institute of Advanced Industrial Science and Technology (AIST), Tsukuba, Japan.

Transmission Electron Microscopy Image Simulations. Representative image simulations were created with the open source SimulaTEM software using an accelerating voltage of 80 kV with Cs = 0.001 mm and −20 nm defocus. Simulation tableau were generated from rotation arrays of the $[Mo_6I_{14}]^{2-}$ ion produced in the commercial program Crystalmaker. Details for image simulation are presented in the Supporting Information.

Raman Spectroscopy. Prior to investigation, the carbon nanotube samples (~0.5 mg) were dispersed in isopropyl alcohol (2 mL) using an ultrasonic bath (~15 min). Subsequently, the dispersion was dropcast onto a Si(100) wafer to support the carbon nanotubes.

The Raman spectra were recorded on a Horiba−Jobin−Yvon LabRAM HR confocal Raman Microscope equipped with a Synapse CCD detector at the Nottingham Nanotechnology and Nanoscience Centre, University of Nottingham. The Raman measurements were performed at room temperature using an excitation laser wavelength of 532 nm operating at a power of ~4 mW (10%) and a 600 lines/mm grating. The Raman shift was calibrated using the Raleigh peak and the 520.7 cm^{-1} silicon line from a Si(100) reference sample.

ASSOCIATED CONTENT

Supporting Information

The Supporting Information is available free of charge on the ACS Publications Web site at DOI: , Video 1 , Video 2 , Video 3 . The Supporting Information is available free of charge on the ACS Publications website at DOI: 10.1021/jacs.6b03633.

HRTEM image simulation, AC-STEM and additional HRTEM and AC-HRTEM imaging, and overall process map of inorganic synthesis in nanotubes (PDF)

Dynamic behavior of tungsten iodide clusters under 80 keV e-beam (AVI)

Dynamic behavior of molybdenum iodide under 80 keV e-beam (AVI)

Transformations of an edge defect in a molybdenum disulfide nanoribbon under 80 keV e-beam (AVI)

AUTHOR INFORMATION

Corresponding Author

*Andrei.Khlobystov@nottingham.ac.uk

Notes

The authors declare no competing financial interest.

DOI: 10.1021/jacs.6b03633
J. Am. Chem. Soc. 2016, 138, 8175−8183

■ ACKNOWLEDGMENTS

J.B. and U.K. acknowledge support of the German Research Foundation (DFG) and the Ministry of Education and Research of the State of Baden-Württemberg within the SALVE project. Z.L. and K.S. acknowledge support of the JST Research Acceleration Program and a Grant-in-Aid for Scientific Research on Innovative Areas (MEXT KAKENHI Grant Number 25107003). A.B., T.W.C., G.A.R., C.S., and A.N.K. acknowledge support of the European Research Council (ERC), the Engineering and Physical Science Research Council (EPSRC), and the Nanoscale & Microscale Research Centre (NMRC) for access to instrumentation.

■ REFERENCES

(1) Britz, D. A.; Khlobystov, A. N. *Chem. Soc. Rev.* **2006**, *35*, 637.
(2) Chuvilin, A.; Khlobystov, A. N.; Obergfell, D.; Haluska, M.; Yang, S.; Roth, S.; Kaiser, U. *Angew. Chem., Int. Ed.* **2010**, *49*, 193.
(3) Koshino, M.; Niimi, Y.; Nakamura, E.; Kataura, H.; Okazaki, T.; Suenaga, K.; Iijima, S. *Nat. Chem.* **2010**, *2*, 117.
(4) Okazaki, T.; Iizumi, Y.; Okubo, S.; Kataura, H.; Liu, Z.; Suenaga, K.; Tahara, Y.; Yudasaka, M.; Okada, S.; Iijima, S. *Angew. Chem., Int. Ed.* **2011**, *50*, 4853.
(5) Botka, B.; Fuestoes, M. E.; Tohati, H. M.; Nemeth, K.; Klupp, G.; Szekrenyes, Z.; Kocsis, D.; Utczas, M.; Szekely, E.; Vaczi, T.; Tarczay, G.; Hackl, R.; Chamberlain, T. W.; Khlobystov, A. N.; Kamaras, K. *Small* **2014**, *10*, 1369.
(6) Chamberlain, T. W.; Biskupek, J.; Rance, G. A.; Chuvilin, A.; Alexander, T. J.; Bichoutskaia, E.; Kaiser, U.; Khlobystov, A. N. *ACS Nano* **2012**, *6*, 3943.
(7) Pollack, A.; Alnemrat, S.; Chamberlain, T. W.; Khlobystov, A. N.; Hooper, J. P.; Osswald, S. *Small* **2014**, *10*, 5077.
(8) Lim, H. E.; Miyata, Y.; Kitaura, R.; Nishimura, Y.; Nishimoto, Y.; Irle, S.; Warner, J. H.; Kataura, H.; Shinohara, H. *Nat. Commun.* **2013**, *4*, 2548.
(9) Nakanishi, Y.; Omachi, H.; Fokina, N. A.; Schreiner, P. R.; Kitaura, R.; Dahl, J. E. P.; Carlson, R. M. K.; Shinohara, H. *Angew. Chem., Int. Ed.* **2015**, *54*, 10802.
(10) Chamberlain, T. W.; Meyer, J. C.; Biskupek, J.; Leschner, J.; Santana, A.; Besley, N. A.; Bichoutskaia, E.; Kaiser, U.; Khlobystov, A. N. *Nat. Chem.* **2011**, *3*, 732.
(11) Britz, D. A.; Khlobystov, A. N.; Porfyrakis, K.; Ardavan, A.; Briggs, G. A. D. *Chem. Commun.* **2005**, 37.
(12) Pagona, G.; Rotas, G.; Khlobystov, A. N.; Chamberlain, T. W.; Porfyrakis, K.; Tagmatarchis, N. *J. Am. Chem. Soc.* **2008**, *130*, 6062.
(13) Allen, C. S.; Ito, Y.; Robertson, A. W.; Shinohara, H.; Warner, J. H. *ACS Nano* **2011**, *5*, 10084.
(14) Chuvilin, A.; Bichoutskaia, E.; Gimenez-Lopez, M. C.; Chamberlain, T. W.; Rance, G. A.; Kuganathan, N.; Biskupek, J.; Kaiser, U.; Khlobystov, A. N. *Nat. Mater.* **2011**, *10*, 687.
(15) Talyzin, A. V.; Anoshkin, I. V.; Krasheninnikov, A. V.; Nieminen, R. M.; Nasibulin, A. G.; Jiang, H.; Kauppinen, E. I. *Nano Lett.* **2011**, *11*, 4352.
(16) Chernov, A. I.; Fedotov, P. V.; Talyzin, A. V.; Lopez, I. S.; Anoshkin, I. V.; Nasibulin, A. G.; Kauppinen, E. I.; Obraztsova, E. D. *ACS Nano* **2013**, *7*, 6346.
(17) Shiozawa, H.; Pichler, T.; Gruneis, A.; Pfeiffer, R.; Kuzmany, H.; Liu, Z.; Suenaga, K.; Kataura, H. *Adv. Mater.* **2008**, *20*, 1443.
(18) Chamberlain, T. W.; Zoberbier, T.; Biskupek, J.; Botos, A.; Kaiser, U.; Khlobystov, A. N. *Chem. Sci.* **2012**, *3*, 1919.
(19) Zoberbier, T.; Chamberlain, T. W.; Biskupek, J.; Kuganathan, N.; Eyhusen, S.; Bichoutskaia, E.; Kaiser, U.; Khlobystov, A. N. *J. Am. Chem. Soc.* **2012**, *134*, 3073.
(20) Lebedeva, I. V.; Chamberlain, T. W.; Popov, A. M.; Knizhnik, A. A.; Zoberbier, T.; Biskupek, J.; Kaiser, U.; Khlobystov, A. N. *Nanoscale* **2014**, *6*, 14877.
(21) Chamberlain, T. W.; Earley, J. H.; Anderson, D. P.; Khlobystov, A. N.; Bourne, R. A. *Chem. Commun.* **2014**, *50*, 5200.
(22) Lu, Y. Z.; Chen, W. *Chem. Soc. Rev.* **2012**, *41*, 3594.
(23) Pan, X.; Bao, X. H. *Acc. Chem. Res.* **2011**, *44*, 553.
(24) Serp, P.; Castillejos, E. *ChemCatChem* **2010**, *2*, 41.
(25) Khlobystov, A. N. *ACS Nano* **2011**, *5*, 9306.
(26) Eliseev, A. A.; Chernysheva, M. V.; Verbitskii, N. I.; Kiseleva, E. A.; Lukashin, A. V.; Tretyakov, Y. D.; Kiselev, N. A.; Zhigalina, O. M.; Zakalyukin, R. M.; Vasiliev, A. L.; Krestinin, A. V.; Hutchison, J. L.; Freitag, B. *Chem. Mater.* **2009**, *21*, 5001.
(27) Song, H.; Ishii, Y.; Al-Zubaidi, A.; Sakai, T.; Kawasaki, S. *Phys. Chem. Chem. Phys.* **2013**, *15*, 5767.
(28) Grigorian, L.; Williams, K.; Fang, S.; Sumanasekera, G.; Loper, A.; Dickey, E.; Pennycook, S.; Eklund, P. *Phys. Rev. Lett.* **1998**, *80*, 5560.
(29) Sloan, J.; Kirkland, A. I.; Hutchison, J. L.; Green, M. L. H. *Acc. Chem. Res.* **2002**, *35*, 1054.
(30) Eliseev, A. A.; Kharlamova, M. V.; Chernysheva, M. V.; Lukashin, A. V.; Tretyakov, Y. D.; Kumskov, A. S.; Kiselev, N. A. *Russ. Chem. Rev.* **2009**, *78*, 833.
(31) Sloan, J.; Matthewman, G.; Dyer-Smith, C.; Sung, A. Y.; Liu, Z.; Suenaga, K.; Kirkland, A. I.; Flahaut, E. *ACS Nano* **2008**, *2*, 966.
(32) Sloan, J.; Liu, Z.; Suenaga, K.; Wilson, N. R.; Pandey, P. A.; Perkins, L. M.; Rourke, J. P.; Shannon, I. J. *Nano Lett.* **2010**, *10*, 4600.
(33) Chamberlain, T. W.; Biskupek, J.; Skowron, S. T.; Bayliss, P. A.; Bichoutskaia, E.; Kaiser, U.; Khlobystov, A. N. *Small* **2015**, *11*, 622.
(34) Skowron, S. T.; Lebedeva, I. V.; Popov, A. M.; Bichoutskaia, E. *Nanoscale* **2013**, *5*, 6677.
(35) Karlin, K. D. *Prog. Inorg. Chem.*; John Wiley & Sons, Inc.: Hoboken, NJ, USA, 2005.
(36) Fedorov, V.; Mishchenko, A.; Fedin, V. *Russ. Chem. Rev.* **1985**, *54*, 408.
(37) Kirakci, K.; Cordier, S.; Shames, A.; Fontaine, B.; Hernandez, O.; Furet, E.; Halet, J. F.; Gautier, R.; Perrin, C. *Chem. - Eur. J.* **2007**, *13*, 9608.
(38) Wang, Z.; Zhao, K.; Li, H.; Liu, Z.; Shi, Z.; Lu, J.; Suenaga, K.; Joung, S. K.; Okazaki, T.; Jin, Z.; Gu, Z.; Gao, Z.; Iijima, S. *J. Mater. Chem.* **2011**, *21*, 171.
(39) Wang, Z.; Li, H.; Liu, Z.; Shi, Z.; Lu, J.; Suenaga, K.; Joung, S. K.; Okazaki, T.; Gu, Z.; Zhou, J.; Gao, Z.; Li, G.; Sanvito, S.; Wang, E.; Iijima, S. *J. Am. Chem. Soc.* **2010**, *132*, 13840.
(40) Kang, J.; Tongay, S.; Zhou, J.; Li, J.; Wu, J. *Appl. Phys. Lett.* **2013**, *102*, 012111.
(41) Serp, P.; Machado, B. *Nanostructured Carbon Materials for Catalysis*; Royal Society of Chemistry: Cambridge, UK, 2015.

DOI: 10.1021/jacs.6b03633
J. Am. Chem. Soc. 2016, 138, 8175−8183